PCCP

An Exact Inversion Method for Extracting Orientation Ordering from Small-Angle Scattering

Journal:	*Physical Chemistry Chemical Physics*
Manuscript ID	CP-ART-11-2020-005886.R1
Article Type:	Paper
Date Submitted by the Author:	08-Jan-2021

Complete List of Authors:	Huang, Guan-Rong; Oak Ridge National Laboratory, Neutron Scattering Division Carrillo, Jan Michael; Oak Ridge National Laboarotry, Wang, Yangyang; Oak Ridge National Laboratory, Center for Nanophase Materials Sciences Do, Changwoo; Oak Ridge National Laboratory, Neutron Scattering Division; Oak Ridge National Laboratory, Biology and Soft Matter Division Porcar, Lionel; Institut Laue-Langevin Sumpter, Bobby; Oak Ridge National Laboratory, Computer Science and Mathematics Division and Center for Nanophase Materials Sci Chen, Wei-Ren; Oak Ridge National Laboratory,

ARTICLE

An Exact Inversion Method for Extracting Orientation Ordering from Small-Angle Scattering

Received 11th November 2020

DOI: 10.1039/x0xx00000x

Guan-Rong Huang*, [a] Jan Michael Carrillo,[b] Yangyang Wang,[b] Changwoo Do,[a] Lionel Porcar,[c] Bobby Sumpter*[b] and Wei-Ren Chen*[a]

We outline a nonparametric inversion strategy for determining the orientation distribution function (ODF) of sheared interacting rods using small-angle scattering techniques. With the presence of direct inter-rod interaction and fluid mechanical forces, the scattering spectra are no longer characterized by the azimuthal symmetry in the coordinates defined by the principal directions of simple shear condition, which severely compounds the reconstruction of ODFs based on currently available methods developed for dilute systems. Using a real spherical harmonic expansion scheme, the real-space ODFs are uniquely determined from the anisotropic scattering spectra and their numerical accuracy are verified computationally. Our method can be generalized to extract ODFs of uniaxially anisotropic objects under different flow conditions in a properly transformed reference frame with suitable basis vectors.

Introduction

For scientific as well as technological reasons, the motion and alignment of flowing rods has been a subject of intense study during the past decades. Extensive computational effort has been dedicated to investigating how the interplay of hydrodynamic forces, Brownian motion, and direct inter-particle interaction influences the orientational ordering of elongated particles under different flow fields. In many industrial processes, anisotropic macromolecules such as stiff polymers[1], nanostructured films[2,3], fibers[4,5], and non-spherical nanoparticles[6,7], are brought into the flow state to create products with specific properties like high modulus or parts with geometrically complex shapes. The effect of flow on the structure–property relationships is an important issue to consider in processing this class of materials.

On the theoretical side, there has been much interest in describing the configuration of suspensions of aligned rods, such as the density functional theory calculation proposed by Onsager.[8] Constitutive modelling or Smoluchowski equation has later been applied to address rod suspensions undergoing flow and deformation.[9-13] In this context, the quantity of interest, through which the effect of orientation entropy, inter-rod exclusion, and long-range interactions on the phase behaviour and rheological response can be delineated, is the orientation distribution function (ODF) of aligned rods,[9-17] partially due to the fact it can be related to a number of important quantities such as the shear and hydrodynamic stresses.[10,18-23] In other words, ODF is of fundamental importance for characterizing the properties and alignment of rod suspensions from the perspective of statistical mechanics.

Various scattering techniques, which render the structural information in terms of two-point spatial correlation functions in reciprocal space, are prominent among the array of experimental tools for measuring ODFs.[4,23-39] Although the experimental protocol can now be routinely implemented under different flow conditions, it is not always straightforward to inversely determine ODFs from the anisotropy of corresponding scattering spectra. It has been recognized that a unique determination of the three-dimensional (3D) real-space ODF can be facilitated by taking advantage of certain angular symmetry of two-dimensional (2D) scattering spectra in reciprocal space in data analysis.[39,40] For example, by analysing the angular symmetry of scattering intensity collected from the plane normal to the incoming beam, determining the preferred orientation of particles in the nematic phase can be conveniently simplified by the axial symmetry with respect to the direction of the flow field.[39-41] However, when suspensions of rodlike objects are subjected to other flow conditions with lower symmetry which are commonly encountered in various industrial processes, the corresponding scattering spectra are known to be characterized by a lower degree of angular symmetries. As a result, extraction of ODFs based on the currently available methods of special analysis is severely compounded. This challenge provides the motivation for this work.

Series expansion is a mathematical scheme for solving mathematical problems whose related functions cannot be expressed explicitly. The approach of spherical harmonics expansion has been commonly adopted by existing experimental and computational studies to facilitate the structural investigation of deforming soft materials.[40-57] Earlier based on the real spherical harmonics expansion (RSHE) we have developed a model-free approach to determine the real-space ODF of suspensions of dilute rods with negligible inter-rod interaction in extensional flows.[40] In

[a] Neutron Scattering Division, Oak Ridge National Laboratory, Oak Ridge, 37831, Tennessee, United States. E-mail: huangrn@ornl.gov; chenw@ornl.gov
[b] Center for Nanophase Materials Sciences, Oak Ridge National Laboratory, Oak Ridge, Tennessee 37831, United States. E-mail: sumpterbg@ornl.gov
[c] Institut Laue-Langevin, B.P. 156, F-38042 Grenoble CEDEX 9, France

this study this facile approach is further generalized to quantitatively determine ODFs of interacting rigid rods aligned by simple steady shear flows. Because of the influence of thermodynamic and hydrodynamic interactions, azimuthal symmetry of scattering spectra collected from the relevant flow planes are no longer preserved. By expanding both scattering intensity and intra-particle spatial correlation in a transformed coordinate system, our nonparametric methodology was able to extract ODFs of aligned rods within the probed range of shear rate without *a priori* assumption of ODF, such as its functional form and boundary condition. The numerical accuracy was further verified by particle-based computer simulations. In related scattering studies, different order parameters are used to provide a quantitative measure of ODF. In what follows we first express the order parameter of ODF (ODF-OP) and scattering order parameter (SOP) in terms of RSHE and show that they can only be related by the RSHE of intra-particle correlation in sufficiently small length scale. We further mathematically demonstrate that reconstruction of ODFs and extraction of the associated ODF-OP can only be achieved by analysing the scattering signal collected from the velocity-velocity gradient plane in a properly rotated reference frame. Complementary dissipative particle dynamics (DPD) simulations were carried out to test the numerical accuracy of our proposed methodology. Our result shows that neither SOP nor the commonly used alignment factor is equal to the ODF-OP for the sheared interacting rods and none of them can provide a quantitative description of ODFs.

Real spherical harmonics expansion (RSHE)

RSHE of orientation distribution function (ODF)

In this study ODF is denoted as $f(\theta,\phi)$. Conventionally, θ and ϕ are respectively the polar and azimuthal angles in a right-handed frame. By RSHE the logarithm of ODF can take the following expression in real space:

$$\ln f(\theta,\phi) = \sum_{l=0}^{\infty}\sum_{m=-l}^{l} \lambda_l^m Y_l^m(\theta,\phi),$$

$$f(\theta,\phi) = \exp[\sum_{l=0}^{\infty}\sum_{m=-l}^{l} \lambda_l^m Y_l^m(\theta,\phi)], (1)$$

where λ_l^m are expansion constants, $Y_l^m(\theta,\phi)$ are the real spherical harmonics (RSH) of order l and degree m satisfying the orthogonal condition: $\int d\Omega\, Y_l^m Y_{l'}^{m'} = 4\pi\delta_{l,l'}\delta_{m,m'}$ and Ω is the solid angle at (θ,ϕ). $\delta_{l,l'}$ and $\delta_{m,m'}$ are the Kronecker delta functions, which are equal to one if subscripts are identical and zero otherwise. For simplicity, $Y_l^m(\theta,\phi)$ is denoted as Y_l^m. Because simple shear flow is symmetrical and it is mathematically convenient, in this work, θ and ϕ are defined as the angles with respect to x- and y-axes, respectively. The directions of flow, velocity gradient, and vorticity are labelled respectively as x, y, and z. From the order parameter of ODF,

$$S_l^m = \frac{1}{4\pi}\int d\Omega\, f(\theta,\phi). (2)$$

A series of integral equations can be generated from Eqn. (2) given the values of $\boldsymbol{S_l^m}$. $\boldsymbol{\lambda_l^m}$ can thus be uniquely determined by these equations when Eqn. (1) is truncated at a finite $\boldsymbol{l}$ value. As shown in the appendix, Eqns. (1) and (2) are equivalent to the ODF with the largest probabilistic entropy subject to certain constraints, and their validity was verified by reconstructing the analytical ODFs in the case studies of uniaxial extension homogenous flow, Kramer's shear flow, and the theory by Doi and Edward.[10] Equation (2) is equivalent to the RSHE of ODF,[40]

$$f(\theta,\phi) = \sum_{l=0}^{\infty}\sum_{m=-l}^{l} S_l^m Y_l^m. (3)$$

When ODF is axially symmetrical along one direction, Eqn. (1) can further be simplified as

$$f(\theta') = \exp\left[\sum_{l=0}^{\infty} \lambda'^0_l Y_l^0(\theta')\right], (4)$$

where θ' is the polar angle in the reference frame where ODF is axially symmetrical to its x-axis and independent of ϕ', and the relation between $(\lambda'^0_l, \lambda_l^m)$ can be determined by the rotation transformation of RSH basis.[40] For simplicity, we denote the lab frame and axially symmetrical ODF frame in Eqn. (1) and Eqn. (4), as "L" and "F", respectively. And the variables with the prime symbol "$'$" are calculated in F, and those without "$'$" are calculated in L.

RSHE of coherent scattering intensity

In this section, we derive the relationship between the anisotropic scattering intensity $I(\boldsymbol{Q})$, order parameter of ODF S_l^m, and scattering order parameter by RSHE, where $\boldsymbol{Q}$ is the momentum transfer of scattered beam. Similarly, $I(\boldsymbol{Q})$ of rigid rods can be expanded as[40-42,56,57]

$$I(\boldsymbol{Q}) = \sum_{l=0}^{\infty}\sum_{m=-l}^{l} I_l^m(Q)\, Y_l^m, (5)$$

where $I_l^m(Q) = \int d\Omega\, I(\boldsymbol{Q}) Y_l^m/(4\pi)$. Because Y_l^m form an orthogonal basis of the Hilbert space of square integrable functions of (θ,ϕ),[58-60] Eqn. (5) is valid for particles with arbitrary shape due to this completeness of Y_l^m.[58-61] It is instructive to indicate the mathematical merits of RSHE for the analysis of $I(\boldsymbol{Q})$: Because ODF is concealed in the angular component of $I(\boldsymbol{Q})$, the spectral analysis can be facilitated by separating the angular variables in terms of Y_l^m. In addition, the parity and angular symmetry of $I(\boldsymbol{Q})$ can be conveniently addressed by Y_l^m due to the periodic nature of trigonometric functions. In scattering experiments, the ODF can be obtained from the angular distribution of $I(\boldsymbol{Q})$, which are $I_l^m(Q)Y_l^m$. For axially symmetrical and elongated particles under uniaxial field, earlier we have demonstrated that the corresponding ODF can be unbiasedly reconstructed from the two-dimensional anisotropic spectra of relevant planes via RSHE.[40]

Scattering order parameter

The scattering order parameter $\hat{S}_l^m(Q)$ has been used to account for the orientational ordering.[4,32,36,62-64] In terms of $I_l^m(Q)$, it can be expressed as

$$\hat{S}_l^m(Q) = \frac{\int d\Omega I(\boldsymbol{Q}) Y_l^m}{\int d\Omega I(\boldsymbol{Q}) Y_0^0} = \frac{I_l^m(Q)}{I_0^0(Q)}. (6)$$

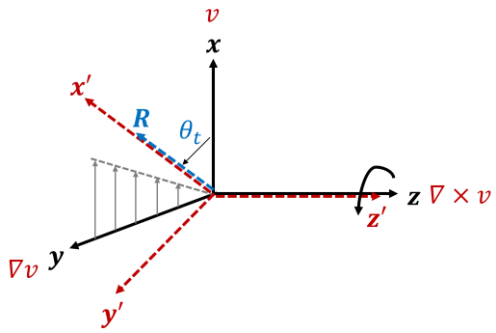

Figure 1. Schematic representation of the xyz-frame (L) and the $x'y'z'$-frame (F), where v is the flow direction. Without loss of generality, we assume the average orientation, $\boldsymbol{R}$, is on the xy-plane with a tilting angle θ_t with respect to the x-axis.

It should be noted that $\hat{S}_l^m(Q)$ is generally not identical to S_l^m. $\hat{S}_l^m(Q)$ defined by $I_l^m(Q)$ in Eqn. (6) is a function of Q while S_l^m defined by ODF in Eqn. (2) is a constant. Without translational periodicity, the scattered intensity from the inter-particle spatial correlation approaches constant in the high Q limit, where the collected scattered intensity is essentially only contributed by the intra-particle correlation. Thus, the experimentally measured $I(\boldsymbol{Q})$ is proportional to the anisotropic single-particle form factor $P(\boldsymbol{Q})$, which is the average of the particle form factor at a specific orientation Ω, $P(\boldsymbol{Q},\Omega)$, with respect to $f(\theta,\phi)$,[40]

$$P(\boldsymbol{Q}) = \sum_{l=0}^{\infty}\sum_{m=-l}^{l} S_l^m P_l^m(Q) Y_l^m(\theta,\phi)\,, \quad (7)$$

where

$$P_l^m(Q) = \frac{1}{16\pi^2}\int d\widehat{\boldsymbol{Q}}\, d\Omega P(\boldsymbol{Q},\Omega) Y_l^m(\Omega) Y_l^m\big(\widehat{\boldsymbol{Q}}\big). \quad (8)$$

$\widehat{\boldsymbol{Q}}$ is the orientation of $\boldsymbol{Q}$. From Eqns. (6) and (7), we can therefore show that in the high Q regime

$$\hat{S}_l^m(Q) = \frac{I_l^m(Q)}{I_0^0(Q)} \approx \frac{P_l^m(Q)}{P_0^0(Q)} S_l^m. \quad (9)$$

In general, $\hat{S}_l^m(Q)$ cannot be uniquely determined from two-dimensional small-angle scattering (SAS) spectra because it is a three-dimensional variable. Unique determination of $\hat{S}_l^m(Q)$ requires additional symmetry or constraints.[40,42] A mathematically tractable approach to circumvent this difficulty is to conduct spectral analysis in a coordinate where the x-axis is along the orientational direction of particles to introduce desired axial symmetry. In this new reference frame F, ϕ is no longer a relevant variable. Only the RSH terms of $m = 0$ in Eqns. (5) and (8) are required for spectral analysis. Therefore, through Eqns. (2) and (4) and the extracted order parameter of ODF from their SAS spectra via Eqns. (8) and (9), ODF of flowing elongated particles can be determined.

ODF reconstruction from coordinate transformation between L and F frames

Here we demonstrate mathematically that the reconstruction of axially symmetrical ODF from RSHE is only feasible by analysing the scattering signal collected from the plane normal to the average orientation of the elongated particles. Considering the configuration in Fig. 1, it can be envisioned that $I(\boldsymbol{Q})$ is axially symmetrical in the reference frame with x'-axis being $\boldsymbol{R}$. This means that we can describe the ODF as a function of only one angular variable, θ'. In high Q regime it can be expressed as

$$I(\boldsymbol{Q}) = A\sum_{l} S'^0_l P_l^0(Q)\, Y_l^0(\Omega'), (10)$$

where A is a constant and

$$f(\theta') = \sum_{l=0}^{\infty} S'^0_l\, Y_l^0(\Omega'). (11)$$

$Y_l^0(\Omega')$ is only a function of $\cos\theta'$ and is proportional to the Legendre polynomial of degree l in terms of $\cos\theta'$. The inner product of $Y_{l_1}^0(\Omega')$ and $Y_{l_2}^0(\Omega')$ satisfies the identity

$$\int_0^{2\pi} d\phi' \int_0^{\pi} d\theta' \sin\theta'\, Y_{l_1}^0(\Omega') Y_{l_2}^0(\Omega') = 4\pi\delta_{l_1,l_2}, (12)$$

where l_1 and l_2 are some integers running from 0 and δ_{l_1,l_2} is again the Kronecker delta function. This means that the orthonormal property is preserved on $x'y'$-plane of F. We can see that F is simply the rotation of L, about the z-axis at an angle θ_t. Therefore, (θ',ϕ') and (θ,ϕ) satisfies the identities:

$$\begin{aligned}\cos\theta' &= \cos\theta_t\cos\theta + \sin\theta_t\sin\theta\cos\phi,\\ \sin\theta'\cos\phi' &= -\sin\theta_t\cos\theta + \sin\theta\cos\phi\cos\theta_t\,, (13)\\ \sin\theta'\sin\phi' &= \sin\theta\sin\phi.\end{aligned}$$

To reconstruct ODF, we at first need to extract S'^0_l from SAS spectra based on Eqns. (9, 10-13). Conventionally, for a simple shear flow, scattering experiments use the Couette flow cell, which can access the spectra on the xy-, xz-, and yz-planes.[42,62] For the sake of simplicity, we denote $I(\boldsymbol{Q})$'s on the xy-, xz-, and yz-planes as $I_{xy}(\boldsymbol{Q})$, $I_{xz}(\boldsymbol{Q})$, and $I_{yz}(\boldsymbol{Q})$, respectively. Via the Eqns. (10) and (13), we can express $I_{xz}(\boldsymbol{Q})$ and $I_{yz}(\boldsymbol{Q})$ as

$$I_{xz}(\boldsymbol{Q}) = A\sum_{l=0}^{\infty} S'^0_l\, P_l^0(Q) Y_l^0(\Omega')$$

$$= A\sum_{l=0}^{\infty} S'^0_l\, P_l^0(Q) Y_l^0(\cos\theta_t\cos\theta), (14)$$

$$I_{yz}(\boldsymbol{Q}) = A\sum_{l=0}^{\infty} S'^0_l\, P_l^0(Q) Y_l^0(\Omega')$$

$$= A\sum_{l=0}^{\infty} S'^0_l\, P_l^0(Q) Y_l^0(\sin\theta_t\cos\phi). (15)$$

Recall that Legendre polynomials are orthogonal functions defined in the domain, $\cos\theta = [-1,1]$. The orthogonal properties are only maintained when $\theta_t = 0$ or π on the xz-plane and $\theta_t = \pi/2$ or $3\pi/2$ on the yz-plane. These happens when the $\boldsymbol{R}$ of elongated particles is along the x- or y-axis. For more general cases, where $\theta_t \in (0,\pi)\setminus\pi/2$, S'^0_l cannot be extracted on both the xz- and yz-planes. Meanwhile, on the xy-plane we have

$$I_{xy}(\boldsymbol{Q}) = A\sum_{l=0}^{\infty} S'^0_l\, P_l^0(Q) Y_l^0(\Omega')$$

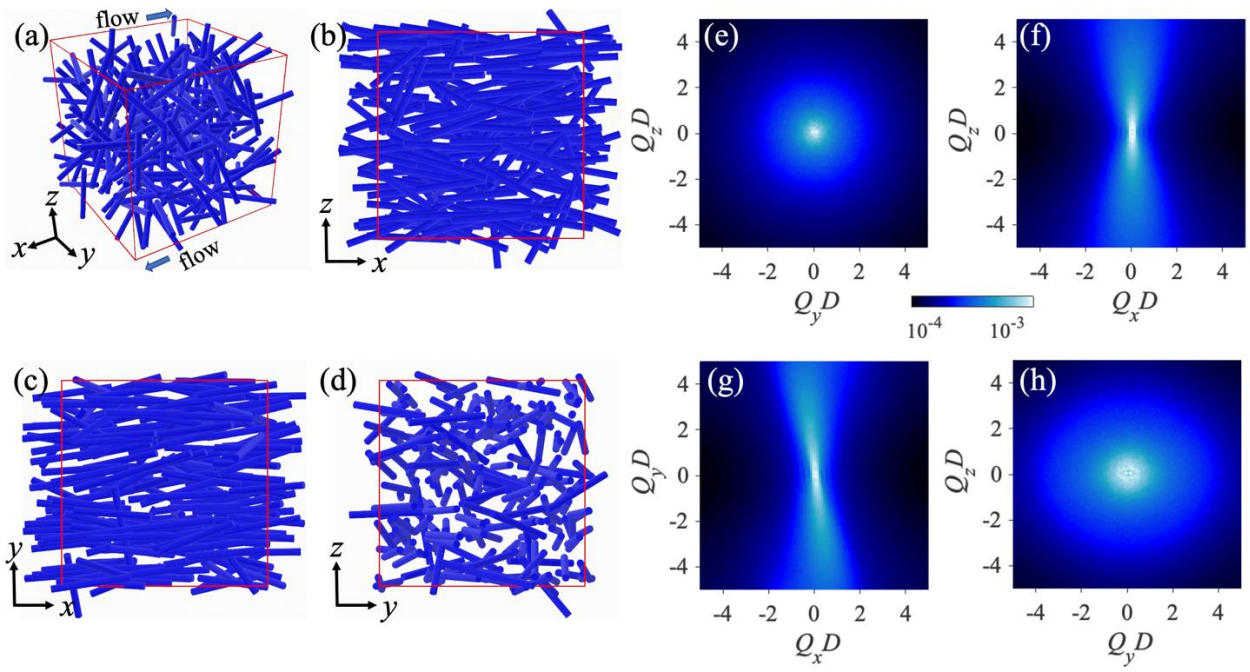

Figure 2. Snapshot of semi-dilute solution of randomly oriented rods with diameter D and length $25D$ in its quiescent state (a) and its corresponding scattering spectra (e). The system consists of 216 rigid rods (blue cylinders) and solvent beads are not shown for clarity. Snapshot of the same solution under high shear with $\mathrm{Pe} = 106.3$ at different projections; flow-vorticity ($x-z$; b), flow-velocity gradient ($x-y$; c), and velocity gradient-vorticity ($y-z$; d) planes. Their corresponding scattering spectra are presented in (f-h), respectively. All the reported scattering spectra are based on ensemble average of 4001 snapshots and were computed through numerical fast Fourier transform. The finite size effect starts to appear around $QL_b \approx 2\pi$ and is insignificant when $QD \geq 1$, where L_b is the size of the simulation box.

$$= A\sum_{l=0}^{\infty} S'^0_l\, P^0_l(Q) Y^0_l(\cos(\theta \pm \theta_t)). \quad (16)$$

In Eqn. (16), the orthogonal properties are kept when l is an even integer. Since most of scattering signatures carry parity symmetry, only the $l = 0, 2, 4, \ldots$ terms remain in the expansion. Subsequently, we can obtain S'^0_l by integrating on the xy-plane

$$S'^0_l = \frac{1}{AP^0_l(Q)} \int_0^{2\pi} \int_{\theta_t}^{\frac{\pi}{2}+\theta_t} d\phi d\theta \sin\theta\, I_{xy}(\boldsymbol{Q}) Y^0_l. \quad (17)$$

To obtain the $P^0_l(Q)$ in Eqn. (17), for the case of rigid rods we can use the following form factor

$$P_{\mathrm{rod}}(\boldsymbol{Q}, \Omega) = \left[j_0\left(\frac{QL_R}{2}\cos\beta\right)\right]^2, \quad (18)$$

where j_0 is the spherical Bessel function of order 0 and β is the angle between the scattering vector $\boldsymbol{Q}$ and the principal axis of a rod. In general, the rod length L_R can be extracted by the model fitting with the scattering intensity of sheared rod suspensions in the quiescent state.

In summary, the step-by-step procedure of ODF reconstruction is given as follows. First, it is to obtain $P^0_l(Q)$ via the spectral decomposition of anisotropic form factor using Eqns. (8) and (18). With $P^0_l(Q)$, we can extract the S'^0_l via Eqns. (9), (14), and (17). Second, calculate λ'^0_l by solving Eqn. (4) with the obtained S'^0_l values to reconstruct $f(\theta')$. Finally, through the coordinate transformation Eqn. (13), the λ^m_l and $f(\theta, \phi)$ can be reconstructed by Eqn. (1).

Dissipative particle dynamics (DPD) simulations of rod suspensions

To demonstrate the validity of the proposed methodology, we perform a series of explicit solvent nonequilibrium molecular dynamics simulations of rods suspensions (see Fig. A2 in the Appendix). Molecular dynamics simulations allow us to access the microstructure evolution of the rods in solution and thereby establish a direct connection to the ensemble-averaged quantities probed in small-angle scattering experiments. It enables us to compare real and reciprocal space analysis of system properties, such as orientational alignment of rods under simple shear. In all the simulations, each rod is modelled by bonded Lennard-Jones (LJ) beads with bead diameter σ and its rigidity is achieved adding a bending potential along its contour. The solvent is made up of non-bonded LJ beads and the concentration of the rod is low enough such that the equilibrium rod orientation distribution is still isotropic (see Fig. A3(b) in the Appendix). The system consists of rods with diameter $D{\sim}\sigma$ and length $L_R{\sim}25D$. The reduced concentrations c explored in this work ranged from $0.02 \leq cL_R^2 D \leq 0.51$, which spans the dilute solution to the semi-dilute regimes (see Table A4 in the Appendix). For dilute case $c \ll L_R^{-3}$ while for semidilute case $L_R^{-3} \leq c \ll D^{-1}L_R^{-2}$.[22] The investigation of different concentration regimes is carried out by coupling the system to a

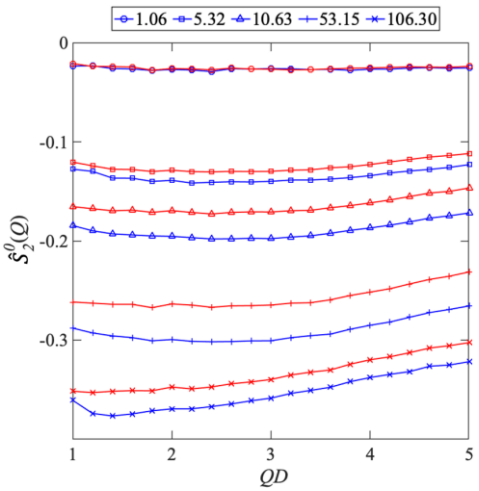

Figure 3. Scattering order parameters $\hat{S}_2^0(Q)$ calculated from the scattering spectra through the trajectories of dissipative particle dynamics simulations consisting of 216 semi-dilute rigid rod suspensions under shear at different values of Pe. Based on Eqn. (6), the blue and red curves were calculated from $I_{xy}(\boldsymbol{Q})$ and $I_{xz}(\boldsymbol{Q})$ spectra, respectively.

dissipative particle dynamics (DPD) thermostat. The DPD thermostat ensures linear and angular momentum conservation, preservation of hydrodynamic interactions on large length scales, and it avoids a temperature profile bias in boundary-driven nonequilibrium simulations of shear flow (see Fig. A4 in the Appendix).[65-69] Shear boundary condition is applied to the system by deforming the triclinic simulation box in the xy-plane, where the shear direction is along the x-axis whereas the velocity gradient is along the y-axis, at different constant shear rates relative to the characteristic time from which a single rod loses its orientational correlation, τ_{Re} (See Table A4 and Fig. A3 for details on τ_{Re} in the Appendix). The applied shear rates, $\dot{\gamma}$, is varied from $10^{-6}\tau^{-1}$ to $10^{-2}\tau^{-1}$ where τ is the characteristic time unit in the simulations. In this study, a dimensionless Peclet number Pe, which is defined as the product of the characteristic end-to-end vector relaxation time of a rod τ_{Re} and the shear rate $\dot{\gamma}$, is used to specify the strength of shear flow and ranged from $10^{-2} \lesssim \mathrm{Pe} \lesssim 10^{2}$. All simulations are performed using LAMMPS.[70-72] Further details of the simulations are presented in the Appendix.

Results and discussion

Small-angle scattering spectra generated from DPD simulations

Figure. 2(a) presents a snapshot of a solution of rods in the semi-dilute regime ($L_R^{-3} < c < L_R^{-2}D^{-1}$) consisting of 216 randomly oriented rigid rods at its quiescent state. Under shear, the flow field disturbs the spatial distribution of rods. Because of the competition between the imposed torque by flow field and rotational diffusion, the alignment of rods driven by the viscous flow would depend on the magnitude of Pe. In Figs. 2(b)-2(d) we present the configurational snapshots of the same system subjected to a shear flow applied along the x direction. Significant orientational ordering at $\mathrm{Pe} = 106.3$ is easily discerned from the projections of the three-dimensional structure on the flow-vorticity ($x-z$; b), flow-velocity gradient ($x-y$; c), and velocity gradient-vorticity ($y-z$; d) planes.

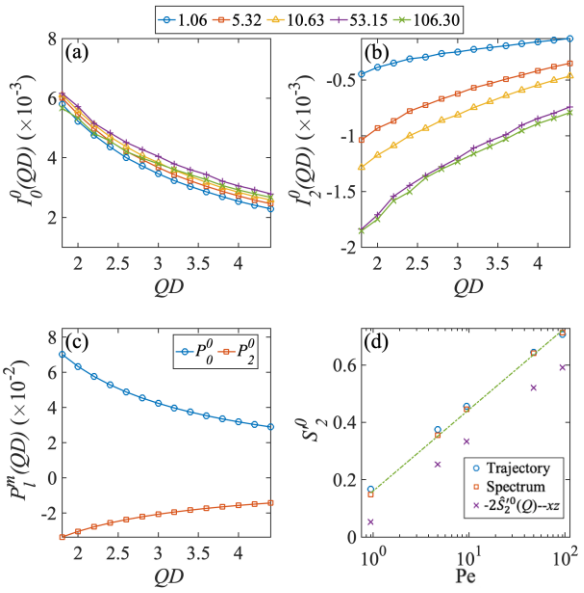

Figure 4. Extracted order parameters of semi-dilute solution consisting of 216 rigid rods under shear at different values of Pe: $I_0^0(QD)$ (a), $I_2^0(QD)$ (b), $P_0^0(QD)$ and $P_2^0(QD)$ (c) using Eqns. (4) and (7). The results of S'^0_2 obtained from spectral analysis, independently obtained from real-space trajectory analysis, and $S'^0_2 = -2\hat{S}'^0_2(Q)$ (obtained from $I_{xz}(\boldsymbol{Q})$) at the limit of $Q \to \infty$ from Eqn. (6) are shown in (d), where $\hat{S}'^0_2(Q)$ were calcualted at the largest probed Q values, $QD \approx 5$.

In Figs. 2(e)-2(h) we show the scattering spectra corresponding to the conformational snapshots given in Figs. 2(a)-2(d).

Analysis of and comparison between S_2^0 and $\hat{S}_2^0(Q)$

In the theoretical calculation of uniaxial nematic phases characterized by azimuthal symmetry, S_2^0 is an important parameter to characterize the system's free energy in predicting the phase transition.[8-17] On the other hand, in many existing SAS experiments[4,32,36,62-64], $\hat{S}_2^0(Q)$ has been calculated from spectral analysis to qualitatively characterize the orientation of rod-like objects aligned by shear flow. It is important to indicate that in diffraction experiments of uniaxial nematic phases of liquid crystals,[38,73] the intensity magnitude is only significant within a narrow Q range. Under this situation, the radial part of intra-particle correlation, $P_0^0(Q)$ and $P_2^0(Q)$ in Eqn. (9), can be adequately approximated as a delta function. The effect of form factor is therefore negligible and the dependence of $\hat{S}_2^0(Q)$ on Q is weak. In this asymptotic condition, it is found that $|S_2^0| \approx |\hat{S}_2^0(Q)|$. However, this equality is generally not held for SAS experiments. In the related studies[4,32,36,62-64] both $I_{xy}(\boldsymbol{Q})$ and $I_{xz}(\boldsymbol{Q})$ are used to calculate $\hat{S}_2^0(Q)$ since both spectra render information of rod alignment with respect to the flow direction x, as indicated by the configurational snapshots given in Figs. 2(b) and 2(c). In Fig. 3 we present the $\hat{S}_2^0(Q)$ obtained from both $I_{xy}(\boldsymbol{Q})$ and $I_{xz}(\boldsymbol{Q})$ spectra which were directly generated from the trajectories at different Pe. Except for the case of $\mathrm{Pe} = 1.06$, a discernible difference between these two $\hat{S}_2^0(Q)$ is observed within the probed Q range. It is also noticeable that this discrepancy exhibits a non-monotonic dependence on Pe. Moreover, upon increasing Pe, the dependence of $\hat{S}_2^0(Q)$ on Q becomes progressively significant. Two factors

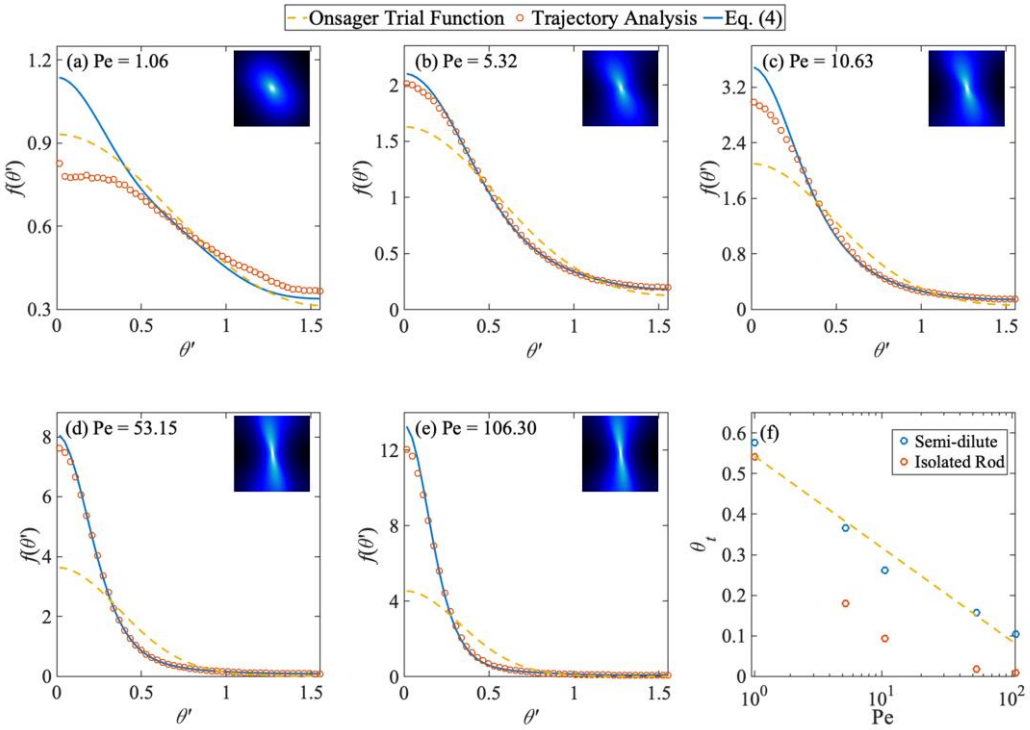

Figure 5. The orientation distribution functions, in the axially symmetrical frame, from dissipative particle dynamics simulations consisting of 216 rigid rods in semi-dilute solution under shear at different values of Pe (a-e). These results were obtained from Onsager trial function (orange dashed lines), real-space trajectory analysis (red circles), and Eqn. (4) (blue solid lines). The inserts in (a-e) are the corresponding $I_{xy}(\boldsymbol{Q})$ scattering spectra. The tilt angles θ_t as a function of Pe for dilute and semi-dilute rod solutions are presented in (f), and the dash line is the best fit straight line. Note that no practical disagreement around $\theta' = 0$, since the factor $\sin\theta'$ needs to take into consideration in a three-dimensional orientation.

account for these observations: As indicated in Eqn. (9), S_2^0 is a dimensionless scalar constant and the dependence of $\hat{S}_2^0(Q)$ on Q comes from the intra-particle spatial correlation. Secondly, as indicated by Figs. 2(d) and 2(h), the azimuthal symmetry of ODF with respect to the flow direction x is no longer preserved, suggesting that the spectra on xy- and xz-planes are not equivalent. Namely, $I(\boldsymbol{Q})$ would be a function of both (θ, ϕ). This is different from the case of axially symmetrical $I(\boldsymbol{Q})$, which is independent of ϕ. To quantitatively reconstruct ODF in real space from the corresponding spectral analysis, these two factors need to be taken into consideration.

To address these issues, we can carry out the spectral analysis in F, where both the ODFs and $I(\boldsymbol{Q})$ are axially symmetrical. F can be obtained by rotating L about z-axis at an angle such that the principal axis of flowing rods coincides with the x-axis of F. This angle is the tilted angle of $I_{xy}(\boldsymbol{Q})$ with respect to the Q_y-axis. As demonstrated by Eqn. (16), $I_{xy}(\boldsymbol{Q})$ can indeed be expressed as a linear combination of Legendre polynomials in terms of new polar angle θ', and accordingly order parameters of ODF can be determined via spectral analysis based on Eqns. (9, 16-18). In Fig. 4 we give the results of spectral decomposition using Eqns. (5) and (6) in F. Figure 4(a) presents the extracted $I_0^0(QD)$, the isotropic component of $I_{xy}(\boldsymbol{Q})$, obtained at different shear rates. $I_0^0(QD)$ are presented in a dimensionless unit QD, and the behaviour of $I_0^0(QD)$ at different Pe values remains almost unchanged within the probed Q range. This observation is expected since $Y_0^0(\Omega')$ basis is independent of angular variables and therefore remains invariant under any rotational operation. The corresponding $I_2^0(QD)$ as a function of Pe are given in Fig. 4(b). Unlike $I_0^0(QD)$, $I_2^0(QD)$ is seen to develop progressively. From Eqns. (6) and (9), this observation indicates a steady increase in ${S'}_2^0$. Figure 4(c) presents the isotropic component of intra-rod spatial correlation $P_0^0(QD)$ and angular component $P_2^0(QD)$ obtained by using Eqns. (8) and (18). For large arguments, $QL_R\cos\beta \gg 1$, in the function $P_{\mathrm{rod}}(\boldsymbol{Q}, \Omega)$, one can show that ${S'}_2^0 \approx -2\hat{S'}_2^0(Q)$.[28,74] Note that this equality holds only when $Q \to \infty$. From the results given in Figs. 4(a) and (c), $\hat{S'}_2^0(Q)$ can be uniquely determined. The results of ${S'}_2^0$ obtained from our proposed approach along with that obtained directly from trajectory analysis and ${S'}_2^0 = -2\hat{S'}_2^0(Q)$ are presented in Fig. 4(d), where $\hat{S'}_2^0(Q)$ were calcualted at the largest probed Q values, $QD \approx 5$.

A quantitative agreement is found between the ${S'}_2^0$ obtained from $I_{xy}(\boldsymbol{Q})$ by our methodology and that independently obtained from configurational calculation of trajectories. This observation demonstrates the rigor and robustness of our methodology in determining ${S'}_2^0$ from two-dimensional spectral analysis. We also notice that in the semi-logarithmic plot, the results follow a straight line. Moreover, as expected, a systematic deviation is found in the ${S'}_2^0$ calculated from $I_{xz}(\boldsymbol{Q})$ in comparison to the ground truth rendered by real space trajectory analysis. Since $I_{yz}(\boldsymbol{Q})$ given in Fig. 2(h) also partially contains the information of axial tilt on the xy-plane, whether ${S'}_2^0$ can be quantitatively calculated based on the information of $I_{xz}(\boldsymbol{Q})$ and $I_{yz}(\boldsymbol{Q})$ presents an intriguing question. However, as demonstrated in Eqns. (14) and (15), due to the lack of

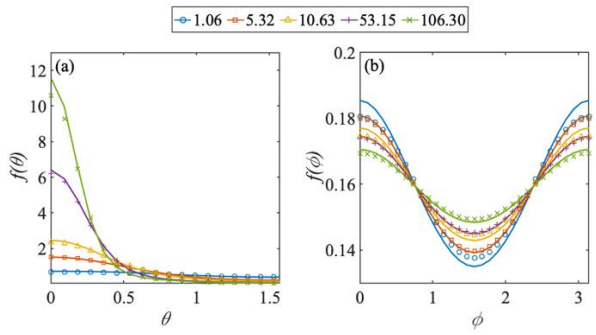

Figure 6. The orientation distribution functions, in the lab frame, obtained from real-space trajectory analysis (symbols) and from the coordinate transformation of $f(\theta')$ in Fig. 5 into Eqn. (1) (solid lines). $f(\theta)$ (a) and $f(\phi)$ (b) are obtained by $\int d\phi f(\theta,\phi)$ and $\int d\theta \sin\theta\, f(\theta,\phi)$, respectively.

suitable orthogonal basis for spectral expansion, coupling between S'^0_2 and other even-order S'^0_l is inevitable and therefore generally S'^0_2 cannot be uniquely determined without the information from $I_{xy}(\boldsymbol{Q})$.

Compare alignment factor $A_f(Q)$ with S_2^0

In this section, we show that it is not possible to connect S_2^0 to commonly used alignment factor $A_f(Q)$, which has been proposed as a measure of molecular orientation for rod-like objects.[75-78] It was claimed that $\lim_{Q\to\infty} A_f(Q) = -S_2^0$. According to its definition, $A_f(Q)$ is found to take the following expression on the xy- and xz-planes:

$$A_f(Q) = \frac{\int_0^{2\pi} d\phi I(\boldsymbol{Q})\cos(2\phi)}{\int_0^{2\pi} d\phi\, I(\boldsymbol{Q})}. \quad (19)$$

Note that in the definition[75-78], ϕ is the azimuthal angle with respect to x-axis, which is different from the definition of this study. Considering the case, where $I(\boldsymbol{Q})$ is axially symmetric to x-axis, the integrand of $A_f(Q)$ can be reduced to $[0,\pi]$. On the xy-plane ϕ is the angle between $\boldsymbol{Q}$ and the flow. Therefore, $I(\boldsymbol{Q})$ can be expressed as

$$I(\boldsymbol{Q}) = \sum_{l=0, l\in even}^{\infty} I_l^0(Q) Y_l^0(\cos\phi), \quad (20)$$

where $I_l^0(Q) = \int_0^{\pi} d\phi \sin\phi\, I(\boldsymbol{Q}) Y_l^0(\cos\phi)/2$. Substituting Eqn. (20) to Eqn. (19), one finds

$$A_f(Q) = 1 - 2\sum_{n=0}^{\infty} \binom{1/2}{n} \frac{\int_0^{\pi} d\phi \sin\phi\, I(\boldsymbol{Q})(-\cos^2\phi)^n}{\int_0^{\pi} d\phi\, I(\boldsymbol{Q})}, \quad (21)$$

where $\binom{1/2}{n}$ is the binomial coefficient. The contribution from $(-\cos^2\phi)^n$ in the integrand on the RHS of Eqn. (21) inevitably contains the information of all $I_l^0(Q)$ with $l \le 2n$. For example, for $n = 1$, it is found to be

$$\frac{\int_0^{\pi} d\phi \sin\phi\, I(\boldsymbol{Q})\cos^2\phi}{\int_0^{\pi} d\phi\, I(\boldsymbol{Q})} = \frac{2}{15}\frac{5I_0^0(Q) - 2I_2^0(Q)}{\int_0^{\pi} d\phi\, I(\boldsymbol{Q})}. \quad (22)$$

Equation (21) clearly demonstrates that, without imposing a specific functional form of ODF, mathematically it is not possible to uniquely determine S_2^0 from $A_f(Q)$. This calculation evidences that $A_f(Q)$ is unable to provide quantitative information about the orientational ordering of aligned rods. It only renders qualitative information as visual inspection of anisotropic spectra.

Comparison between Onsager trial functions and ODFs from the trajectory analysis in simulation

Having demonstrated that our approach produces reliable estimates of S'^0_2 by taking full advantage of angular symmetry via transformation of coordinates, we now can readily examine the connection between S'^0_2 and ODF as a function of Pe. Such results are presented in Fig. 5. In this figure, each ODF is presented in terms of the polar angle distribution function $f(\theta') \equiv \int d\phi' f(\theta',\phi')$ along the principal axis. Note that (θ',ϕ') are the angles in F. From the corresponding $I_{xy}(\boldsymbol{Q})$ given in the insert, a steady decrease of ODFs in θ' upon increasing in Pe is clearly seen. In addition, the spectrum becomes more anisotropic. In existing studies of rigid rod systems under field alignment or shear flow, S_2^0 has been used as a dominant parameter to characterize the ODF of aligning rods, including Onsager Theory[8], Smoluchowski theory[39,62], Maier-Saupe theory[62,63,79], and Doi-Edwards theory[10]. In theoretical cases, their ODFs can be expressed analytically as a function of S_2^0. For a given value of S_2^0, the functional behaviors of those ODFs are similar to each other. Therefore, we choose the Onsager's trial function $\Psi_O(\theta) = \alpha\cosh(\alpha\cos\theta)/(4\pi\sinh\alpha)$ as a comparison with the ODFs of aligned rods obtained from our simulation results. The parameter α is related to S_2^0 by: $S_2^0 = 1 + 3\alpha^{-2} - 3\alpha^{-1}\coth\alpha$. With those corresponding S'^0_2 given in Fig. 4, $f(\theta')$ at different Pe calculated from $\Psi_O(\theta')$ is given by the dashed lines in Fig. 5. In comparison to the $f(\theta')$ directly obtained from trajectory analysis given by the circle symbols, the difference becomes more significant at higher shear rates. The validity of $\Psi_O(\theta')$ is to describe the transition of nematic phase in terms of the alignment of dilute rigid rod suspensions, where the orientation of any tagged rod is nearly independent from that of other constituent rods in the system. Under such a condition, S'^0_2 alone is adequate for capturing the transition characteristics. However, in our simulated semi-dilute rod suspensions undergoing steady simple shear flow, the orientation of a single rod is profoundly influenced by its interactions with other rods. Therefore, the observed disagreement in Fig. 5 is therefore not a surprise.

Reconstruction of ODF from anisotropic SAS spectra by RSHE

Instead of proposing an alternative theory of ODF, the focus of this work is placed on extracting ODF from spectral anisotropy. The harder question of whether under the shear flow condition S'^0_2 is sufficient to determine the corresponding ODF of aligned rods in real space has not been answered unambiguously. In fact, we have found that dependence of anisotropic spectra around the principal axis on polar angle θ' cannot be satisfactorily described by $(3\cos^2\theta' - 1)/2$ alone, which suggests higher-order components of

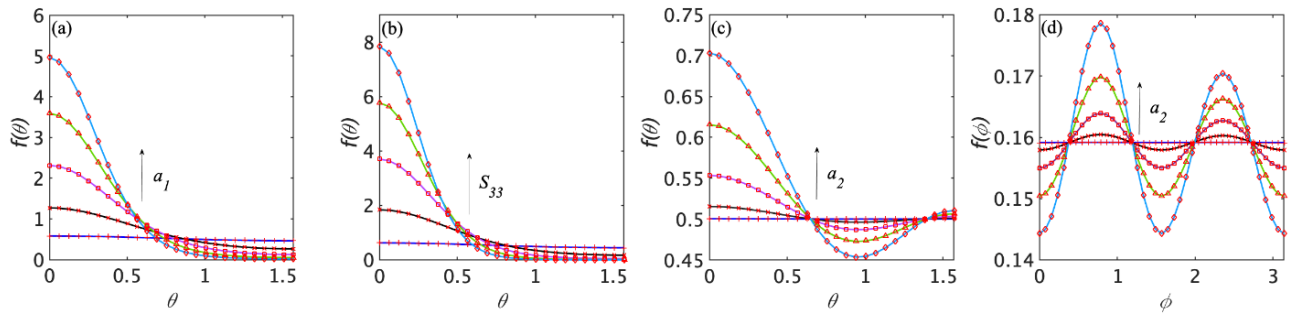

Figure A1. The comparison between the ODFs of the uniaxial extension homogeneous flow, Doi-Edwards theory, and Kramer's simple homogeneous flow, and the ODF reconstruction based on information theory. The symbols and solid lines are the results of ODF reconstruction by Eqns. (1, 2) and Eqn. (A4), respectively. λ_l^m, a_1, a_2, and S_{33} are listed in the following tables A1, A2, and A3.

S'^0_l are required to quantitatively determine ODF of sheared rods from $I_{xy}(\boldsymbol{Q})$ through Eqns. (8), (9) and (17). Based on the logarithmic expansion of ODF in terms of RSH basis, we propose an approach to quantitatively determine ODF from spectral analysis through Eqns. (4), (8), (9), (17), and (18). In Fig. 5, the $f(\theta')$ determined from our proposed methodology of spectral analysis (solid curves) indeed agrees well with the ground truths determined from the real-space trajectory analysis of simulation data within the probed range of Pe. Note that no practical disagreement around $\theta' = 0$, since the scale factor $\sin\theta'$ in a solid angle needs to take into consideration. The universal quantitative agreement verifies the feasibility of our approach. The results presented in Fig. 5 clearly show that for a system of interacting rigid rods subjected to shear stresses, S'^0_2 only reflects qualitative information of averaged rod alignment. By transforming the $f(\theta')$ in Fig. 5 from F to L coordinate, using Eqns. (1) and (13), the information of ODFs can be presented as a function of θ and ϕ angles (Fig. 6). The overall agreement is consistent with Fig. 5, except for the small deviation in ϕ orientation. Moreover, from the semi-logarithmic plot presented in Fig. 5(f), the tilt angle θ_t, which is the angle between the average direction of rods and flow direction, exhibits a nearly logarithmically decay on Pe, which is intrinsically different from the expectation of an isolated rod rotating affinely in a shear flow. We attribute this difference to the influence of various inter-rod interactions including excluded volume and hydrodynamic interactions. This also shows that the high order S_l^m cannot be ignored and S_2^0 is insufficient for quantitatively determining the ODF of aligned rods observed in this study.

Conclusions

In summary, this work demonstrates the validity of ODF reconstruction by RSHE through a direct comparison with the DPD simulations of semi-dilute rigid rod suspensions undergoing a simple shear flow at different values of Pe. We clarify that the commonly used scattering parameter $\hat{S}_l^m(Q)$ and alignment factor $A_f(Q)$ cannot provide quantitative information of orientational ordering. Our proposed methodology successfully reconstructs the ODFs from spectral analysis of the anisotropic scattering spectra. Furthermore, we show that the commonly used order parameter of ODF S_2^0 is inadequate for providing a quantitative description of ODF due to the presence of strong interactions at the molecular level and intra-particle spatial correlation. Because of the orthogonality loss of basis functions on the detector plane, three-dimensional ODF can only be determined from the flow planes on which the axial symmetry of spectra can be retrieved by rotating the coordinate axis. For particles with irregular shapes, this specific flow plane may not be accessible by the current Couette shear flow cells, therefore, it is helpful to construct a shear flow apparatus allowing for assessment of SAS spectra on multiple planes. Finally, with the availability of suitable sample environments and access to the relevant flow planes, the current methodology could be generalized to quantitatively address other collective orientational motions such as kayaking, wagging, and rolling observed in shear flow or other orientational phenomena occurring in other flows conditions. Thereby this work provides a valuable benchmarking to facilitate the related studies of deforming soft materials in theory and simulation computation, using scattering techniques.

Appendix

Benchmark between the ODF reconstruction by Eqns. (1) and (2) and analytical ODFs

The expression of Eqn. (1) also can be obtained by maximizing the probabilistic entropy,[55,80] which can be defined as

$$-\langle \ln f(\theta,\phi)\rangle = -\int d\Omega f(\theta,\phi)\ln f(\theta,\phi)\,, \text{(A1)}$$

where $\langle \dots \rangle$ pertains to the average with respect to $f(\theta,\phi)$. Based on the method of Lagrange multiplier, we can maximize the objective function,

$$H = -\langle \ln f(\theta,\phi)\rangle + \sum_{l,m}\lambda_l^m[\langle Y_l^m(\theta,\phi)\rangle - S_l^m]\,, \text{(A2)}$$

where the constant λ_l^m is the Lagrange multiplier for the S_l^m constraint. To maximize H, we can perform functional derivatives on H with respect to f and set it to zero

$$0 = \frac{\delta H}{\delta f(\theta,\phi)} = \langle -1 - \ln f(\theta,\phi) + \sum_{l,m}\lambda_l^m Y_l^m(\theta,\phi)\rangle\,. \text{(A3)}$$

This equality clearly holds when the quantity inside the bracket $\langle \dots \rangle$ is zero, and $f(\theta,\phi)$ satisfies the constraint equations of S_l^m. Therefore, the ODF reproduces the expression of Eqn. (1) subject to Eqn. (2) constraints.

Here we benchmark the ODF reconstruction via Eqn. (1) and Eqn. (2) constraints with some case studies of flowing rods whose

a_1	0.05	0.35	0.65	0.95	1.25
λ_0^0	-2.30e-3	-1.19e-1	-4.19e-1	-8.89e-1	-1.46e0
λ_2^0	6.71e-2	4.70e-1	8.72e-1	1.27e0	1.68e0
λ_4^0	9.20e-9	1.09e-7	7.32e-12	8.20e-8	1.76e-8
λ_6^0	8.84e-9	9.94e-8	-4.60e-12	3.01e-10	-1.10e-8
λ_8^0	7.77e-9	1.25e-7	-2.08e-11	-3.24e-9	4.07e-9

Table A1. Uniaxial extension homogenous flow. The parameters of ODF reconstruction calculated by Eqn. (1) subject to Eqn. (2) constraints with order parameters of ODF, S_0^0, S_2^0, S_4^0, S_6^0 and S_8^0, obtained from Eqn. (A4).

S_{33}	0.05	0.35	0.65	0.95	1.25
λ_0^0	-5.21e-3	-2.72e-1	-9.23e-1	-1.83e0	-2.87e0
λ_2^0	1.01e-1	7.04e-1	1.31e0	1.91e0	2.52e0
λ_4^0	9.36e-10	4.27e-14	-1.03e-8	1.30e-12	2.87e-13
λ_6^0	8.99e-10	3.61e-14	-2.37e-8	-8.73e-13	-1.35e-13
λ_8^0	8.11e-10	6.09e-14	1.65e-8	3.52e-13	4.04e-14

Table A2. Doi-Edwards ODF. The parameters of ODF reconstruction calculated by Eqn. (1) subject to Eqn. (2) constraints with order parameters of ODF, S_0^0, S_2^0, S_4^0, S_6^0, and S_8^0, obtained from Eqn. (A4), $S_{11} = S_{22} = -S_{33}/2$ and $U = 1$.

ODFs can be expressed analytically in the flow fields: uniaxial extension homogeneous flow, Doi-Edwards ODF, Kramer's shear flow. These ODFs take the following forms, respectively,

$$f(\theta,\phi) = \frac{1}{J}\exp[\frac{3a_1}{\sqrt{5}}Y_2^0(\theta,\phi)],$$

$$f(\theta,\phi) = \frac{1}{J}\exp\left[\frac{3U}{2}u_\alpha u_\beta S_{\alpha\beta}\right], \quad \text{(A4)}$$

$$f(\theta,\phi) = \frac{1}{J}\exp[\frac{3a_2}{\sqrt{15}}Y_2^{-2}(\theta,\phi)],$$

where J^{-1} is the normalization constant, $a_1 = \dot{\epsilon}/(6D_r)$, $a_2 = \dot{\lambda}/(6D_r)$, D_r is the rotation diffusion coefficient, $\dot{\epsilon}$ and $\dot{\lambda}$ are shear rate and tensile rate, U is a constant related to inter-rod interaction, u_α is the α component of unit vector along rod direction, and $S_{\alpha\beta} = \langle u_\alpha u_\beta - 1/3\rangle$ is the second rank order tensor. Noted that for the case of Doi-Edwards ODF we only take the diagonal terms since one can always rotate the reference and make $S_{\alpha\beta}$ diagonal. Figure A1 gives the results of ODF reconstruction, where red cross markers and blue lines are calculated by Eqns. (1, 2) and (A4), respectively. We integrated $f(\theta,\phi)$ with respect to θ or ϕ for the ease of comparison. Namely, $f(\theta) \equiv \int d\phi f(\theta,\phi)$ and $f(\phi) \equiv \int d\theta \sin\theta\ f(\theta,\phi)$. Overall, there is no discernible difference observed between them. The reconstruction data for λ_l^m are also given in the following Tables A1, A2, and A3. It is clearly that for all the case studies of ODFs in Eqn. (A4) λ_l^m terms with $l > 2$ are negligible and consistent with their functional form. Since λ_l^m is inside the exponential function in Eqn. (1), ODF will be always dominated by the λ_l^m terms with largest values.

a_2	0.05	0.35	0.65	0.95	1.25
λ_0^0	-2.53e0	-2.54e0	-2.56e0	-2.59e0	-2.63e0
λ_2^0	4.43e-11	4.34e-9	1.21e-9	3.91e-10	-1.20e-10
λ_2^{-2}	3.87e-2	2.71e-1	5.0e-1	7.36e-1	9.68e-1
λ_4^0	4.93e-11	4.64e-9	1.37e-9	3.40e-10	-2.31e-10
λ_4^{-2}	1.10e-9	3.38e-8	6.61e-9	-3.96e-10	4.91e-10
λ_4^4	1.08e-6	-1.61e-7	-6.01e-8	-3.29e-8	4.13e-9
λ_6^0	4.71e-11	4.44e-9	8.10e-10	3.32e-12	-1.87e-11
λ_6^{-2}	2.55e-9	5.79e-8	1.09e-8	-8.54e-10	6.72e-10
λ_8^0	4.07e-11	4.13e-9	8.42e-10	5.25e-12	-6.68e-12
λ_8^{-2}	7.92e-10	8.20e-8	1.80e-8	1.04e-11	6.26e-12

Table A3. Kramer's simple homogeneous flow. The parameters of ODF reconstruction calculated by Eqn. (1) subject to Eqn. (2) constraints with order parameters of ODF, S_0^0, S_2^0, S_2^{-2}, S_4^0, S_4^{-2}, S_4^4, S_6^0, S_6^{-2}, S_8^0 and S_8^{-2}, obtained from Eqn. (A4).

Simulation details and trajectory

Below, we describe the molecular dynamics simulations of rods under simple shear. The simulation consists of N_R number of rods with explicit solvent. We modeled a rod as 50 connected Lennard-Jones (LJ) beads connected by anharmonic bonds and kept straight and rigid by imposing a bending potential to two neighbouring bonds. The solvent is represented as a single LJ bead. The non-bonded pair-wise interaction is described by a truncated and shifted LJ potential,

$$U_{LJ}(r) = \begin{cases} 4\varepsilon_{LJ}\left[\left(\frac{b}{r_{ij}}\right)^{12} - \left(\frac{b}{r_{ij}}\right)^{6} - \left(\frac{b}{r_{cut}}\right)^{12} + \left(\frac{b}{r_{cut}}\right)^{6}\right] & r < r_{cut}, \\ 0 & r \geq r_{cut} \end{cases} \quad \text{(A5)}$$

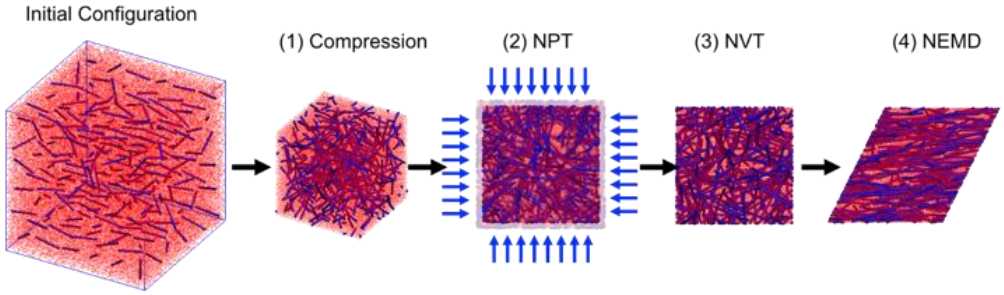

Figure A2. Molecular dynamics (MD) simulation protocol of rods (blue beads) in solution (red beads). The initial configuration is compressed to a final total number density of $0.85\sigma^3$(step 1), then NPT simulation was performed at a set pressure of $8.45k_BT/\sigma^3$(step 2), then NVT simulation is performed at the volume equal to the average volume of the NPT simulation (step 3). Finally, NEMD simulation is performed by deforming the simulation box at a constant shear rate, $\dot{\gamma}$ (step 4).

N_R	$N_{solvent}$	N_{total}	$L(\sigma)$	cL_R^2D	$\tau_{Re}(\tau)$	β_{Re}
8	240150	240550	65.44	0.02	9126	0.982
27	235996	237346	65.10	0.06	8040	1.065
64	243340	246540	65.83	0.14	8498	0.998
125	236323	242573	65.30	0.27	10594	0.925
216	222558	233358	64.19	0.51	10629	1.067
432	218015	239615	64.16	1.02	16816	0.991
512	213530	239130	63.88	1.22	19828	0.967
729	197576	234026	62.51	1.83	57929	0.840
1000	189249	239249	61.66	2.58	465875	0.804

Table A4. System sizes and characteristic times. N_R is the number of rods, $N_{solvent}$ is the number solvent beads, N_{total} is the total number of beads, L is the equilibrium box size, cL_R^2D is the normalized concentration, τ_{Re} is the characteristic time of the stretch exponential decay function, and β_{Re} is the stretching exponent.

where r_{ij}, is the distance between the i^{th} and j^{th} bead, ε_{LJ} is the well depth and r_{cut} is the cutoff and equal to $b2^{1/6}$. The bead size, b, for the rod-to-rod is $b=\sigma$, for the rod-to-solvent is $b=0.9\sigma$ and for the solvent-to-solvent is $b=\sigma$, where b is expressed in units of σ. The ε_{LJ} between all LJ interactions is set to 1 k_BT where k_BT is the thermal energy. The connectivity of rod beads was maintained by the finite extension nonlinear elastic (FENE) potential,[81]

$$U_{FENE}(r) = -\frac{1}{2}k_sR_m^2\ln\left(1-\frac{r^2}{R_m^2}\right)+4\varepsilon_{LJ}\left[\left(\frac{\sigma_f}{r_{ij}}\right)^{12}-\left(\frac{\sigma_f}{r_{ij}}\right)^{6}\right], \text{(A6)}$$

with the spring constant $k_s=30k_BT/\sigma^2$, maximum bond length $R_m=1.5\sigma$, and $\sigma_f=0.4753\sigma$ such that the minimum of $U_{FENE}(r)$ is at $r=0.5\sigma$. A bending potential,

$$U_{i,i+1}^{bend} = k_BTK_a\left(1-(\vec{n}_i\cdot\vec{n}_{i+1})\right), \text{(A7)}$$

was included to promote rod rigidity, with $K_a=2000$ for consecutive unit bond vectors $\vec{n}_i$ and $\vec{n}_{i+1}$. In this model, the persistence length of the rod, l_p, is very much higher than its length ($l_p \gg \langle R\rangle^{\frac{1}{2}}\sim 25\sigma$). The pair-wise interaction, $U_{LJ}(r)$, was evaluated for all beads except for bead-to-bead interactions that are bonded and those that are within two bonds away. A constant temperature of $T=1.0$ was maintained by coupling the system to a dissipative particle dynamics (DPD) thermostat implemented in LAMMPS.[70-72] In this case, the force on the i^{th} particle exerted by the j^{th} particle is

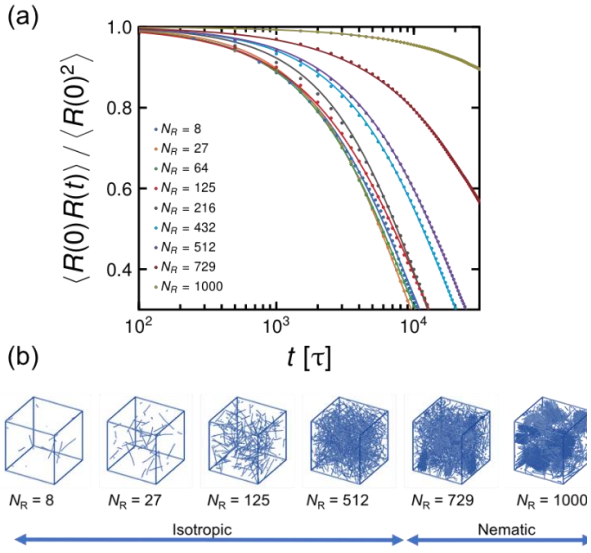

Figure A3. End-to-end vector autocorrelation function, $\frac{\langle\vec{R}(0)\cdot\vec{R}(t)\rangle}{\langle\vec{R}^2(0)\rangle}$ (a) and snapshots of simulations at different rod concentrations (b).

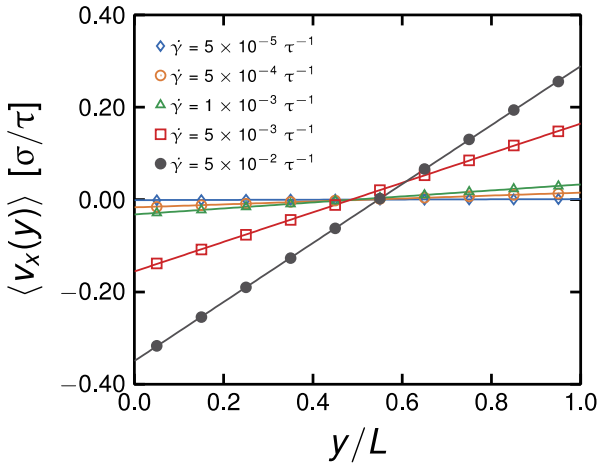

Figure A4. Velocity profile of N_R=216 system at different shear rates.

$$m\frac{d\vec{v}_i(t)}{dt} = (F(t)^C + F(t)^D + F(t)^R)\hat{r}_{ij}, \qquad \text{(A8)}$$

where m is the mass of a particle and is set to 1; $\hat{r}_{ij}$ is a unit vector in the r_i-r_j direction; $F(t)^C$ is the conservative force defined in Eqns. (A5-7); $F(t)^D$is the dissipative force with $F(t)^D = -\gamma\left(1-\frac{r_{ij}}{r_c}\right)^2(\hat{r}_{ij}\cdot\vec{v}_{ij})$, where $\vec{v}_{ij}$ is the difference in velocities of the two particles, $r_c=2.5\sigma$ is the cutoff, and $\gamma=k_BT\tau/\sigma^2$ is the dissipation coefficient; and $F(t)^R$ is a random force with $F(t)^R=(2k_BT\gamma)^{\frac{1}{2}}\left(1-\frac{r_{ij}}{r_c}\right)\alpha(\Delta t)^{-1/2}$, where Δt is the integration timestep and is equal to 0.005τ, τ is the characteristic time and defined as $\tau=\sigma(m/k_BT)^{1/2}$, α is a Gaussian random number with zero mean and unity variance. The velocity-Verlet algorithm is used for the time integration.

The simulation protocol consisted of four steps: (1) Initial setup and compression of the simulations box, (2) Isobaric-isothermal (NPT) ensemble simulation, (3) Canonical (NVT) ensemble simulation, and (4) Non-equilibrium MD simulation – simulations under constant shear rate. In step (1), rods are initially arranged in a square lattice with random orientation and then the simulation box is compressed for a time interval of $5\times10^3\ \tau$ such that the final total number density is $0.85\sigma^3$. In step (2), NPT ensemble simulation is performed using a Berendsen barostat with a setpoint pressure of $8.45k_BT/\sigma^3$ and a time interval of $5\times10^4\ \tau$. In step

(3), rods are allowed to relax at a time interval of $2 \times 10^5\ \tau$, and we determined the characteristic time from which the end-to-end vector loses correlation, τ_{Re}, based on the decay of its autocorrelation function. In step (4), we deform the simulation box at a constant shear rate ranging from $\dot{\gamma} = 1 \times 10^{-6}\ \tau^{1/2}$ to $\dot{\gamma} = 1 \times 10^{-2}\ \tau^{1/2}$ at a time interval of $5 \times 10^5\ \tau$. The simulation steps are illustrated in Fig. A2 and the system sizes and equilibrium box sizes in step 3 are listed in Tab. A4.

In step (3) of Fig. A2, we determine the characteristic time from which the end-to-end vector of a rod, $\vec{R}$, loses correlation by calculating $\langle \vec{R}(0) \cdot \vec{R}(t) \rangle / \langle \vec{R}^2(0) \rangle$ and then we fit the data points with a stretched exponential $\frac{\langle \vec{R}(0) \cdot \vec{R}(t) \rangle}{\langle \vec{R}^2(0) \rangle} = \exp\left(-(t/\tau_{Re})^{\beta_{Re}}\right)$. The results of these procedures are shown in Fig. A3(a) and tabulated in Tab. A4. Note that in Fig. A3(a), there is a sudden increase in the characteristic time of $\langle \vec{R}(0) \cdot \vec{R}(t) \rangle / \langle \vec{R}^2(0) \rangle$ for N_R=512 to N_R=729 suggesting a change from an isotropic to a nematic phase in the solution as seen in the snapshots of Fig. A3(b). We limited our non-equilibrium MD simulation (step 4) to systems that are in the isotropic phase. In step 4, the simulation box is deformed where shearing is done in the xy-plane, the direction of the velocity is along the x-axis and the velocity gradient is along the y-axis. In Fig. A4, the velocity profile of the beads follows a linear profile with the velocity at the bottom and at the top are $-L\dot{\gamma}/2$ and $L\dot{\gamma}/2$, respectively.

Conflicts of interest

There are no conflicts to declare.

Acknowledgements

This research was supported by the Laboratory Directed Research and Development Program of Oak Ridge National Laboratory, managed by UT-Battelle, LLC, for the U.S. Department of Energy, and performed at SNS, which is DOE Office of Science User Facilities operated by the Oak Ridge National Laboratory. Y.W. acknowledges support by the U.S. Department of Energy (DOE), Office of Science, Office of Basic Energy Sciences, Early Career Research Program Award KC0402010, under Contract DE-AC05-00OR22725. Molecular dynamics simulations were conducted at the Center for Nanophase Materials Sciences, which is a DOE Office of Science User Facility. This research used resources of the Oak Ridge Leadership Computing Facility, which is supported by the Office of Science of the U.S. Department of Energy under Contract DE-AC05-00OR22725.

This manuscript has been authored by UT-Battelle, LLC under Contract No. DE-AC05-00OR22725 with the U.S. Department of Energy. The United States Government retains and the publisher, by accepting the article for publication, acknowledges that the United States Government retains a non-exclusive, paid-up, irrevocable, worldwide license to publish or reproduce the published form of this manuscript, or allow others to do so, for United States Government purposes. The Department of Energy will provide public access to these results of federally sponsored research in accordance with the DOE Public Access Plan (http://energy.gov/downloads/doe-public-access-plan).

References

1 S. Gantenbein, K. Masania and W. Woigk *et al.*, *Nature*, 2018**, 561**, 226–230.
2 Y.-Z. Long, M. Yu, B. Sun, C.-Z. Gu and Z. Fan, *Chem. Soc. Rev.*, 2012, **41**, 4560–4580.
3 R. Blell, X. Lin, T. Lindström, M. Ankerfors, M. Pauly, O. Felix and G. Decher, *ACS Nano*, 2016, **11**, 84–94.
4 K. M. O. Håkansson, A. B. Fall, F. Lundell, S. Yu, C. Krywka, S. V. Roth, G. Santoro, M. Kvick, L. P. Wittberg, L. Wågberg *et al.*, *Nat. Commun.*, 2014, **5**, 4018.
5 M. Richard-Lacroix and C. Pellerin, *Macromolecules*, 2013 46(24), 9473-9493.
6 N. Patil, L. Balzano, G. Portale and S. Rastogi, *Macromolecules*, 2010 43(16), 6749-6759.
7 Y. Wu, Z. Jiang, X. Zan, Y. Lin and Q. Wang, *Colloids Surf. B*, 2017, **158**, 620–626.
8 L. Onsager, *Ann. N. Y. Acad. Sci.*, 1949, **51**, 627–659.
9 See Chapter 2 of P. G. de Gennes and J. Prost, *The Physics of Liquid Crystals*; Clarendon Press, 1993, and the references therein.
10 M. Doi and S. F. Edwards, *The Theory of Polymer Dynamics*; Oxford University Press, 1986.
11 See Chapter 10 of R. G. Larson, *Constitutive Equations for Polymer Melts and Solutions*; Butterworth-Heinemann Press, 1988, and the references therein.
12 See Chapter 14 of R. B. Bird, C. F. Curtiss, R. C. Armstrong and O. Hassager, *Dynamics of Polymeric Liquids: Kinetic Theory*; John Wiley and Sons: New York, 1987; Vol. 2., and the references therein.
13 H. G. Jerrard, *Chem. Rev.*, 1959, **59**, 345-428.
14 H. He, E. M. Sevick and D. R. M. Williams, *J. Chem. Phys.*, 2016, *144*, 124901.
15 T. Odijk, *Macromolecules*, 1986, **19**, 2313–2329.
16 J. Herzfeld, A. E. Berger and J. W. Wingate, *Macromolecules*, 1984, **17**, 1718–1723.
17 W. M. Gelbart and B. A. Baron, *J. Chem. Phys.*, 1977, **66**, 207–221.
18 G. K. Batchelor, *J. Fluid Mech.* 1970, **41**, 545–570.
19 M. Rahnama and D. L. Koch*, Physics of Fluids*, 1995, **7**, 487
20 C. A. Stover, D. L. Koch and C. Cohen, *J. Fluid Mech.*, 1992, **238**, 277-296.
21 F. Folgar and C. L. Tucker, *J. Reinf. Plast. Compos.*,1984, **3**(2), 98-119.
22 J. E. Butler and B. Snook, *Annu. Rev. of Fluid Mech.*, 2018, **50**, 299-318
23 J. B. Hayter and J. Penfold, *J. Phys. Chem.*, 1984, **88**, 4589–4593.
24 R. J. Fox, W.-R. Chen, C. Do, J. P. Stephen, M. G. Forest and T. J. Dingemans, *Rheol. Acta*, 2020*,* **59***,* 727-743.
25 D. W. Hayward, J. B. Gilroy, P. A. Rupar, L. Chabanne, C. Pizzey, M. A. Winnik, G. R. Whittell, I. Manners and R. M. Richardson, *Macromolecules*, 2015, **48**(5), 1579–1591.
26 M. Gopinadhan, P. W. Majewski, Y. Choo and C. O. Osuji, *Phys. Rev. Lett.*, 2013, **110**, 078301.
27 J. Wagner, C. Märkert, B. Fischer and L. Müller, *Phys. Rev. Lett.*, 2013, **110**, 048301.
28 J. B. Gilroy, P. A. Rupar, G. R. Whittell, L. Chabanne, N. J. Terrill, M. A. Winnik, I. Manners and R. M. Richardson, *J. Am. Chem. Soc.*, 2011, **133**, 17056–7062.
29 C. Märkert, B. Fischer and J. Wagner, *J. Appl. Crystallogr.*, 2011, **44**, 441–447.
30 J. Viamontes, S. Narayanan, A. R. Sandy and J. X. Tang, *Phys. Rev. E*, 2006, **73**, 061901.
31 K. R. Purdy, Z. Dogic, S. Fraden, A. Rühm, L. Lurio and S. G. J. Mochrie, *Phys. Rev. E*, 2003, **67**, 031708.
32 V. M. Ugaz and W. R. Burghardt, *Macromolecules*, 1998, **31**, 8474–8484.

33 W. Orts, L. Godbout, R. H. Marchessault and J. F. Revol, *Macromolecules*, 1998, **31**, 5717–5725.
34 C. M. Chen and G. G. Warr, *Langmuir*, 1997, **13**, 1374−1376.
35 S. M. King, R. K. Heenan, V. M. Cloke and C. Washington, *Macromolecules*, 1997, **30**, 6215–6222.
36 K. Hongladarom, V. M. Ugaz, D. K. Cinader, W. R. Burghardt, J. P. Quintana, B. S. Hsiao, M. D. Dadmun, W. A. Hamilton and P. D. Butler, *Macromolecules*, 1996, **29**, 5346–5355.
37 J. Penfold, E. Staples and P. G. Cummins, *Adv. in Colloid and Interface Sci.*, 1991, **34**, 451-476.
38 A. J. Leadbetter and E. K. Norris, *Mol. Phys.*, 1979, **38**, 669–686.
39 T. Rosén, C. Brouzet, S. V. Roth, F. Lundell and L. D. Söderberg, *J. Phys. Chem. C*, 2018, **122**(12), 6889–6899.
40 G.-R. Huang, Y. Wang, C. Do, Y. Shinohara, T. Egami, L. Porcar, Y. Liu and W.-R. Chen, *ACS Macro Lett.*, 2019, **8**, 1257-1262.
41 G.-R. Huang, Y. Wang, B. Wu, Z. Wang, C. Do, G. S. Smith, W. Bras, L. Porcar, P. Falus and W.-R. Chen, *Phys. Rev. E*, 2017, **96**, 022612.
42 Z. Wang, C. N. Lam, W.-R. Chen, W. Wang, J. Liu, Y. Liu, L. Porcar, C. B. Stanley, Z. Zhao, K. Hong and Y. Wang, *Phys. Rev. X*, 2017, **7**, 031003.
43 D. J. Evans, H. J. M. Hanley and S. Hess, *Phys. Today*, 1984, **37**, 1, 26.
44 D. J. Evans and H. J. M. Hanley, *Phys. Rev. A*, 1979, **20**, 1648.
45 H. J. M. Hanley and D. J. Evans, *J. Chem. Phys.*, 1982, **76**, 3225.
46 S. Hess and H. J. M. Hanley, *Phys. Rev. A*, 1982, **25**, 1801.
47 H. J. M. Hanley, J. C. Rainwater and S. Hess, *Phys. Rev. A*, 1987, **36**, 1795.
48 F. Morris and B. Katyal, *Phys. Fluids*, 2002, **14**, 1920.
49 J. A. Pryde, *The Liquid State*; Hutchison University Library: London, 1966.
50 W. T. Ashurst and W. G. Hoover, *Phys. Rev. A:* 1975, **11**, 658−678.
51 D. J. Evens and G. Morriss, *Statistical Mechanics of Nonequilibrium Liquids*; Cambridge University Library: Cambridge, 2008.
52 S. J. Johnson, C. G. de Kruif and R. P. May, *J. Chem. Phys.*, 1988, **89**, 5909−5921.
53 N. J. Wagner and W. B. Russel, *Phys. Fluids A*, 1990, **2**, 491–502.
54 N. J. Wagner and B. J. Ackerson, *J. Chem. Phys.*, 1992, 97, 1473−1483.
55 M. van Gurp, *Colloid Polym. Sci.* 1995, **273**, 607–625.
56 G.-R. Huang, Y. Wang, B. Wu and W.-R. Chen, *Phys. Rev. E*, 2018, **97**, 012605.
57 G.-R. Huang, Y. Wang, C. Do, L. Porcar, Y. Shinohara, T. Egami and W.-R. Chen, *J. Phys. Chem. Lett.*, 2019, **10**(14), 3978-3984.
58 G. B. Arfken and Hans J. Weber, *Mathematical Methods for Physicists*; 4th ed., Academic Press, Orlando, 1995.
59 R. Shankar, *Principles of Quantum Mechanics*; 2nd ed., Plenum, New York, 1994.
60 J. D. Jackson, *Classical Electrodynamics*, Wiley, New York, 1962.
61 G. Strang, *Introduction to Linear Algebra*; 4th ed., Wellesley-Cambridge Press, 2009.
62 C. Lang, J. Kohlbrecher, L. Porcar, A. Radulescu, K. Sellinghoff, J. K. G. Dhont and M. P. Lettinga, *Macromolecules*, 2019, **52**, 9604–9612.
63 X. Chen, C. Burger, D. Fang, B. S. Hsiao and B. Chu, *Polymer*, 2006, **47**, 2839.
64 K. M. O. Håkansson, F. Lundell, L. Prahl-Wittberg and L. D. Söderberg, *J. Phys. Chem. B*, 2016, **120**, 6674–6686.
65 R. D. Groot and P. B. Warren, *J. Chem. Phys.*, 1997, **107**(11), 4423–4435.
66 T. Soddemann, B. Dunweg and K. Kremer, *Phys. Rev. E*, 2003, **68**, 04670.
67 J. M. V. A. Koelman and P. J. Hoogerbrugge, *Europhys. Lett.*, 1993, **21**, 363–368.
68 P. Espanol and P. Warren, *Europhys. Lett.*, 1995, **30**, 191–196.
69 I. Pagonabarraga, M. H. J. Hagen and D. Frenkel, *Europhys. Lett.*, 1998, **42**, 377–382.
70 W. M. Brown, P. Wang, S. J. Plimpton and A. N. Tharrington, *Comput. Phys. Commun.*, 2011, **182**, 898–911.
71 S. J. Plimpton, *J. Comput. Phys.*, 1995, **117**, 1–19.
72 T. D. Nguyen and S. J. Plimpton, *Comput. Mater. Sci.*, 2015, **100**, 173–180.
73 D. M. Agra-Kooijman, M. R. Fish and S. Kumar, *Liq. Cryst.*, 2018, **45**(5), 680-686
74 R. Lovell and G. R. Mitchell, *Acta Cryst.*, 1981, **37**, 135-137.
75 L. M. Walker, W. A. Kernick III and N. J. Wagner, *Macromolecules* 1996, **29**, 2298-2301.
76 L. M. Walker, W. A. Kernick III and N. J. Wagner, *Macromolecules* 1997, **30**, 508-514.
77 M. E. Helgeson, P. A. Vasquez, E. W. Kaler and N. J. Wagner, *J. Rheol.* 2009, **53**(3), 727-756.
78 J. D. Park, K. H. Ahn and N. J. Wagner, *J. Rheol.* 2016, **61**(1), 117-137.
79 G. R. Luckhurst and C. Zannoni, *Nature*, 1977, **267**, 412–414.
80 M. Kardar, *Statistical Physics of Particles*, Cambridge University Press, Cambridge, UK, 2007.
81 K. Kremer, *J. Chem. Phys.*, 1990, **92**, 5057-5086.